





RESEARCH ARTICLE OPEN ACCESS

Considerations on the XPS Analysis of 2H-TaS₂ (0001)Charalampos Drivas^{1,2,3}  | C. Richard A. Catlow^{1,2,4}  | Mark A. Isaacs^{4,5}  | Georgios Kyriakou³ 

¹Cardiff Catalysis Institute, School of Chemistry, Cardiff University, Cardiff, UK | ²UK Catalysis HUB, Research Complex at Harwell, Science and Technology Facilities Council, Rutherford Appleton Laboratory, Didcot, UK | ³Department of Chemical Engineering, University of Patras, Rion, Greece | ⁴Department of Chemistry, University College London, London, UK | ⁵Harwell XPS, Research Complex at Harwell, Science and Technology Facilities Council, Rutherford Appleton Laboratory, Didcot, UK

Correspondence: Charalampos Drivas (c.drivas@upatras.gr)**Received:** 27 June 2025 | **Revised:** 11 August 2025 | **Accepted:** 18 August 2025**Funding:** The research work was supported by the Hellenic Foundation for Research and Innovation (HFRI) under the HFRI PhD Fellowship Grant (Fellowship Number: 673) and Engineering and Physical Sciences Research Council (EP/Y023587/1, EP/Y023609/1, EP/Y023536/1, EP/Y023552/1, EP/Y023544/1, EP/R026939/1, EP/R026815/1, EP/R026645/1, and EP/R027129/1).**Keywords:** asymmetry | quantification | TaS₂ | XPS

ABSTRACT

A 2H-TaS₂ (0001) single crystal was studied with XPS. The quantification and fitting procedures for this material are discussed in detail. It is shown that conventional approaches for data deconvolution fail, and an in-depth analysis utilising theoretical sensitivity factors and taking into account the shake-up and loss structures is needed to produce accurate results. Additionally, the inherent asymmetry of the Ta and S peaks is highlighted, and appropriate line shapes are determined.

1 | Introduction

Transition metal dichalcogenides (TMDs) have attracted much attention over the last few years [1] due to their 2D nature, as van der Waals structures, for various applications ranging from catalysis [2–6] and microelectronics [7–11] to superconductivity [12–14]. The 2H polymorph of TaS₂ is a promising material due to its metallic characteristics [15], exotic correlated quantum states [16], superconductivity [12, 17], and catalytic properties [6, 18].

XPS is one of the most widely used techniques for the study of TMDs due to its inherent surface sensitivity and qualitative, quantitative, and electronic information it can provide. While XPS of 2H-TaS₂ has been reported since the 1970s [19], there has not been a detailed study that properly deconvolutes the spectra. This material is particularly interesting because it is metallic, but not an elemental metal, and as such it should have asymmetric peaks [20–22], which is true for both the Ta and S peaks.

Moreover, TMDs are known for the presence of both bulk and surface plasmons [23], which need to be considered for accurate fitting and quantification. However, an overview of the 2H-TaS₂ XPS spectra reported in 2024 reveals major problems in the analysis [24–30], not only disregarding the aforementioned asymmetry, but also inappropriate backgrounds and spin-orbit splitting components. Given the importance of understanding the Ta environment in materials, it is of utmost importance to set a solid foundation for its characterisation. We therefore examine carefully the fitting process and quantification for all Ta and S core levels for a 2H-TaS₂ (0001) single crystal.

2 | Experimental

A synthetic single crystal of 2H-TaS₂ was purchased from HQ Graphene. Before introducing it to the ultrahigh vacuum (UHV) chamber, it was mechanically exfoliated in an Ar glovebox using a double-sided copper tape, which was also used for mounting

This is an open access article under the terms of the [Creative Commons Attribution](https://creativecommons.org/licenses/by/4.0/) License, which permits use, distribution and reproduction in any medium, provided the original work is properly cited.

© 2025 The Author(s). *Surface and Interface Analysis* published by John Wiley & Sons Ltd.

the crystal on the holder, and then transferred in an inert atmosphere, minimising contamination. No further treatment was performed to avoid sample degradation [31].

All XPS data were acquired using a Kratos Axis SUPRA using a monochromated Al K α X-ray source (1486.69 eV) at 17 mA emission and 15 kV HT (255 W – unless otherwise stated) and an analysis area of 700 \times 300 μ m. The instrument was calibrated to gold metal Au 4f_{7/2} (83.96 eV) and dispersion adjusted to give a Binding Energy (BE) of 932.62 eV for the Cu 2p_{3/2} line of metallic copper. The Ag 3d_{5/2} line FWHM at 10 eV pass energy was 0.54 eV. Source resolution for monochromatic Al K α X-rays was \sim 0.3 eV. The instrumental resolution was determined to be 0.29 eV at 10 eV pass energy using the Fermi edge of the valence band for metallic silver. Instrument resolution with the charge compensation system on was determined to be $<$ 1.33 eV FWHM on PTFE. All core level spectra were collected with a PE of 20 eV, while the survey scan was at 160 eV.

Data analysis was performed using CasaXPS 2.3.26rev1.2V. A Shirley background was used for all regions, except Ta 4s, where an offset Shirley background was used. For the core level peaks, the LF line shape was used, while the rest were fitted using Voigt-like line shapes. The LF line shape is a modified version of the LA function and is defined by four parameters: LF(α , β , w , m). The parameters α and β control the Lorentzian asymmetry on the high- and low-binding energy sides of the peak, respectively. w is a damping factor that accounts for the finite background window, and m defines the Gaussian broadening. For further details, readers are referred to the CasaXPS manual, which is publicly available. For the quantification, both Scofield and Kratos RSFs were used, after correcting for the electron analyser transmission function exponential factor ($N=0$) and the X-ray angular distribution (source-analyser angle = 54°).

3 | Results and Discussion

The wide scan spectrum was initially recorded, Figure 1a, to check the sample purity. Only small amounts of carbon and oxygen were present, indicating a successful exfoliation and sample transfer procedure. High-resolution spectra of all the regions are presented in Figure 1b–h. It is evident that all the detected signals display a certain degree of asymmetry, which is expected, as mentioned previously. It is worth highlighting the observed asymmetry for the S 2p, S 2s, and S 3s peaks, which, while it has been established in the literature [32–34], is rarely regarded in the analysis of metallic TMDs.

The Ta 4f region, Figure 1f, shows some additional features at higher BEs, more specifically at around 26 and 28 eV. These features are an inherent property of certain samples and represent an excess of intercalated TaO_x species [19]. While they are present in all Ta orbitals, because of their low intensity and overlap with other spectral features, fitting was not performed to discern them. In the S 2p region (Figure 1e), additional features near the main peak are observed that are not attributable to peak asymmetry. These components have been labeled as surface-related species and may correspond to polysulphides, surface sulphides, Ta–S–O compounds, bridging sites, or S-terminated domains introduced during exfoliation [35–39], which are most likely

intrinsic to the surface. Although their contribution is relatively minor—accounting for approximately 8% of the total sulphur signal—they must be considered during peak fitting to ensure accuracy. However, they do not significantly affect the overall results presented in this work. To fit the experimental data accurately, a quantification analysis was first carried out. For this purpose, a conventional approach was used, where the regions noted on Figure 1b–d, e insert, and f (for the S 2s region, the loss feature was not taken into account) and the RSF provided by Kratos were utilised. The quantification results, summarised in Table 1 under the conventional approach column, indicate that there is a significant excess of sulphur in the sample, taking of course into account that a small portion of the detected Ta is in the form of TaO_x species. Moreover, the Ta 4s and Ta 4p regions are not 1:1 with the Ta 4f peak. To solve this problem, theoretical (Scofield) RSFs were used, along with wider regions to entail any loss features. These loss features are due to plasmons and valence band and core-level excitations [40]. The results obtained under these analysis conditions are summarised in Table 1 under the losses fitting column. Evidently, this approach works better for this system as all the Ta regions appear to have an area ratio of 1. The S over Ta ratio is 1.85, slightly below 2, as expected. Utilising this information, the Ta 4f region was deconvoluted, as shown in Figure 1f.

Fitting of the Ta 4f loss region requires us to also fit the Ta 5p and 5s signals. For the Ta 5p orbital, the 5p_{3/2} component is well separated from the loss features and is used to constrain the area, $\frac{1}{2}$ ratio, and position, +9.26 eV, of the 5p_{1/2} spin-orbit split peak. No meaningful results could be obtained by fixing both the area ratio and the FWHM, so only the area ratio was used, suspecting the presence of a Coster-Kronig transition [41]. Considering the Ta 5s, the position was constrained according to Bearden et al. [42] and the area according to Ta 4f, Ta 4f: Ta 5s ratio is 24.59. For the fitting of the Ta 4f losses, the fewest number of peaks was used, 5, without any constraints. Additionally, loss features for the Ta 5p and 5s orbitals are expected, but no fitting was used to discern these. For quantification purposes, however, the loss features of the 5p orbital were estimated to be 0.42 times the deconvoluted area, while for the 5s orbital this is 0.52 times.

Fitting the Ta 4d and S 2s region is challenging due to the overlap of the corresponding peaks. To address this, the Ta 4d_{3/2} component was used to constrain the 4d_{5/2} orbital, allowing the remaining intensity in the region to be attributed to the S 2s peak. Further support for this assignment comes from the observed energy separation between the S 2s and S 2p_{3/2} levels, which matches that of both single-crystal and CVD-grown MoS₂ samples [10, 11]. Regarding loss features, metallic tantalum typically exhibits two broad plasmon-related losses [43], whereas the S 2s loss structure is expected to resemble that of the S 2p region. Accordingly, three peaks were used to model the loss features in this region: two for Ta 4d and one for S 2s. The tantalum loss peaks were constrained to have comparable FWHM and energy separations to those observed for the spin-orbit components of Ta 4d. In contrast, the position of the sulphur loss peak was not constrained, as a distinct spectral feature is present, and its fitted position agrees well with the S 2p loss structure. The selected fitting range also accommodates higher-binding-energy loss features that are not fully resolved, and this approach is further justified by the quantification results.

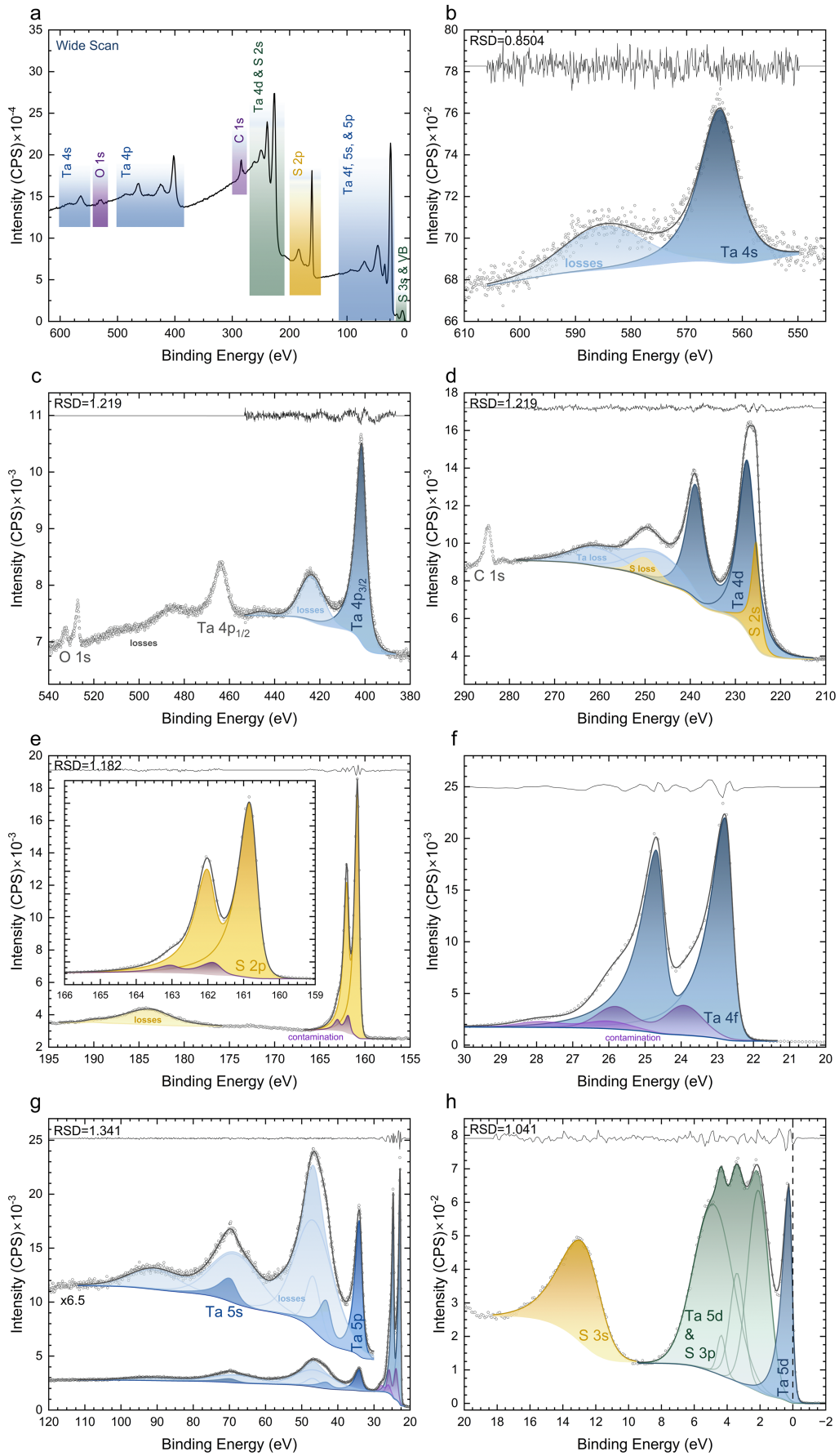


FIGURE 1 | XPS spectra of all the measured regions with the proposed fittings. (a) Wide scan, (b) Ta 4s, (c) Ta 4p and O 1s, (d) Ta 4d, S 2s, and C 1s, (e) S 2p, (f) Ta 4f, (g) Ta 4f, Ta 5p, and Ta 5s, (h) S 3s and valence band.

TABLE 1 | Quantification of the 2H-TaS₂ single crystal using the two different approaches discussed.

	Losses fitting			Conventional approach		
	Area (CPs x eV)	RSF (Scofield)	Area/Ta 4f	Area (CPs x eV)	RSF (Kratos)	Area/Ta 4f
Ta 4s	11,534.2	1.440	0.94	11,534.2	0.244	3.12
Ta 4p	57,544.6	6.529	1.04	57,544.6	3.266	1.16
Ta 4d	128,080.3	16.327	0.93	128,080.3	5.192	1.72
Ta 4f	86,745.1	10.231	1.00	47,026.0	3.109	1.00
Ta 5s	3684.7	0.416	1.04	—	N/A	—
Ta 5p	12,886.0	1.288	1.18	—	N/A	—
S 2s	23,740.5	1.484	1.89	16,717.0	0.391	2.83
S 2p	28,658.1	1.829	1.85/2.05 ^a	21,482.4	0.673	2.10/2.58 ^a
S 3s	1037.0	0.173	0.70	—	N/A	—
O 1s	2174.3	2.427	0.10	2174.3	0.780	0.10
C 1s	3795.9	1.000	0.45	3795.9	0.278	0.49

^aSubtracting contamination.

TABLE 2 | Fitting parameters used for all the regions measured.

	Position (eV)	Relative area	FWHM (eV)	Line shape
Ta 4s				
4s	564.00	1 (7,411.9)	7.40	LF(1.5,2,20,0)
Loss	+20.93	0.556	16.98	GL(30)
Ta 4p				
4p _{3/2}	401.49	1 (26,947.7)	5.04	LF(1.1,1.7,20,0)
Loss 1	+22.08	0.396	12.32	GL(30)
Loss 2	+43.91	0.028	9.08	GL(30)
Ta 4d				
4d _{5/2}	227.40	1 (53,913.4)	4.64	LF(1.5,1.5,20,0)
4d _{3/2}	+11.50	0.667	4.64	LF(1.5,1.5,20,0)
Loss 1	+19.75	0.428	13.19	GL(30)
Loss 2	+35.51	0.282	13.70	GL(30)
S 2s				
2s	225.38	1 (16,712.5)	1.94	LF(1.1,1.7,30,0)
Loss	+24.44	0.421	6.23	GL(30)
S 2p				
2p _{3/2}	160.81	1 (13,251.1)	0.47	LF(0.9,2.5,25,25)
2p _{1/2}	+1.20	0.500	0.47	LF(0.9,2.5,25,25)
(contamination) 2p _{3/2}	+1.02	0.081	0.53	LF(0.9,2.5,25,25)
(contamination) 2p _{1/2}	+2.22	0.040	0.53	LF(0.9,2.5,25,25)
Loss 1	+23.00	0.530	5.58	LF(1,1.5,4,0)
Loss 2	+29.26	0.010	1.74	GL(30)

(Continues)

TABLE 2 | (Continued)

	Position (eV)	Relative area	FWHM (eV)	Line shape
Ta 4f				
4f _{7/2}	22.76	1 (22,051.3)	0.44	LF(0.8,4,20,10)
4f _{5/2}	+1.91	0.750	0.44	LF(0.8,4,20,10)
(contamination) 4f _{7/2}	+1.16	0.177	1.18	GL(30)
(contamination) 4f _{5/2}	+3.07	0.133	1.18	GL(30)
(contamination) 4f _{7/2}	+3.25	0.054	1.42	GL(30)
(contamination) 4f _{5/2}	+5.16	0.041	1.42	GL(30)
Loss 1	+23.66	1.022	12.16	GL(30)
Loss 2	+24.13	0.166	4.42	GL(30)
Loss 3	+34.49	0.022	3.87	GL(30)
Loss 4	+45.49	0.578	15.39	GL(30)
Loss 5	+68.07	0.234	16.09	GL(30)
Ta 5p				
5p _{3/2}	34.07	1 (6,003.9)	1.87	LF(1.1,2.5,15,0)
5p _{1/2}	+9.26	0.50	3.18	LF(1.1,2.5,15,0)
Ta 5s				
5s	69.86	1 (2,203.2)	4.34	LF(1.1,2.5,15,0)
S 3s				
3s	12.55	1 (991.4)	2.52	LF(1.2,5,3,50)
Valence band				
Ta 5d	0.22	1 (556.5)	0.43	LF(1.1,5,10,0)
VB 1	+1.88	1.735	1.50	GL(30)
VB 2	+3.16	0.710	1.05	GL(30)
VB 3	+4.13	0.148	0.59	GL(30)
VB 4	+4.61	2.705	2.82	GL(30)

Notably, variations in the high-BE endpoint have minimal influence on the core-level peak fitting and primarily affect the representation of the loss features. It should be mentioned that the only peak area that does not agree with the quantification results is the S 3s, which is significantly smaller than expected, which may be due to the 3s orbitals being part of the Valence Band [44] for which no loss features were taken into account and potential overlap with O 2s and C 2s orbitals. The Valence Band consists of Ta 5d and S 3p mixed orbitals, while the VB edge is mostly attributed to the Ta 5d orbital [44]. Fitting was performed to represent the envelope with the smallest number of peaks, as shown in Figure 1h. The fitting results for all the regions are summarised in Table 2.

Overall, the differences between the two approaches may be due to a number of contributing factors. The first, and most likely, is that the most important reason for the observed differences when analysing Ta is that the loss features are not taken into account, as is frequently done with other elements [45]. With regard to the experimental RSFs, while the original papers [46, 47]

list the values, the exact regions used were not mentioned, so in this respect there may be some inconsistencies. Finally, the presence of contaminants on the surface affects the quantification of the peaks and the determination of the experimental RSF values, which are typically obtained from samples with a small degree of contamination.

4 | Conclusions

A single crystal of the basal plane of 2H-TaS₂ was examined by XPS. It was shown that conventional approaches for quantification of the peaks fail, and a more thorough approach is necessary to obtain accurate results. It was shown that due to the metallic nature of the material, all peaks displayed asymmetric features, and their line shapes were determined, which is especially important for the S orbitals because they rarely display such features. Based on the present results and the described methodology, future analysis of TaS₂ by analysts can lead to a more accurate understanding of the physical system.

While this work presents a detailed analysis of all spectral regions, such an approach is often not practical for routine analysis of common samples containing 2H-TaS₂, where the material is typically present in low concentrations and thus produces weak XPS signals. For sulfur analysis, the S 2p peak is recommended, as it is well-resolved and free from significant overlap. For tantalum, the Ta 4f orbitals are generally the most reliable starting point; however, in oxygen-rich environments, the Ta 4d or even Ta 4p_{3/2} orbitals may provide more accurate information, depending on the spectral quality.

When performing quantification using experimental RSFs and standard background subtraction methods, sulfur content is typically overestimated by approximately 30%. For systems where a high degree of precision is not required, conventional methods may still be employed—with the sulfur overestimation clearly noted. In cases demanding more accurate quantification, the use of Scofield RSFs, fitting of only the main components, and application of relative loss feature ratios (as listed in Table 2) are recommended to obtain reliable peak areas.

Finally, as the intensity and position of loss features depend on the sample's crystallinity and the electronic structure of its valence and conduction bands, they may also serve as qualitative indicators of surface modification, such as oxidation. However, in systems with low crystallinity, plasmon loss features are typically less pronounced, and the fitting strategies outlined here should be applied with caution.

Author Contributions

C.D.: conceptualisation, data curation, formal analysis, visualisation, writing – original draft preparation. **C.D., C.R.A.C., and M.A.I.:** funding acquisition. **C.R.A.C., M.A.I., and G.K.:** writing – review and editing.

Acknowledgements

The research work was supported by the Hellenic Foundation for Research and Innovation (HFRI) under the HFRI PhD Fellowship grant (Fellowship Number: 673). XPS analysis was performed at the EPSRC UK National Facility for XPS - HarwellXPS (grants EP/Y023587/1, EP/Y023609/1, EP/Y023536/1, EP/Y023552/1 and EP/Y023544/1). The UK Catalysis Hub is kindly thanked for resources and support provided via our membership of the UK Catalysis Hub Consortium and funded by EPSRC (grants EP/R026939/1, EP/R026815/1, EP/R026645/1 and EP/R027129/1).

Conflicts of Interest

The authors declare no conflicts of interest.

Data Availability Statement

Information on the data underpinning this publication, including access details, is openly available in the Cardiff University Research Data Repository at doi.org/10.17035/cardiff.29957861.

References

1. S. Aftab, M. Z. Iqbal, and Y. S. Rim, “Recent Advances in Rolling 2D TMDs Nanosheets Into 1D TMDs Nanotubes/Nanoscrolls,” *Small* 19, no. 1 (2023): 2205418, <https://doi.org/10.1002/sml.202205418>.

2. E. Kovalska, P. K. Roy, N. Antonatos, et al., “Photocatalytic Activity of Twist-Angle Stacked 2D TaS₂,” *npj 2D Materials and Applications* 5, no. 1 (2021): 68, <https://doi.org/10.1038/s41699-021-00247-8>.
3. Y. Sim, Y. Chae, and S. Y. Kwon, “Recent Advances in Metallic Transition Metal Dichalcogenides as Electrocatalysts for Hydrogen Evolution Reaction,” *iScience* 25, no. 10 (2022): 105098, <https://doi.org/10.1016/j.isci.2022.105098>.
4. Y. Yang, H. Fei, G. Ruan, C. Xiang, and J. M. Tour, “Edge-Oriented MoS₂ Nanoporous Films as Flexible Electrodes for Hydrogen Evolution Reactions and Supercapacitor Devices,” *Advanced Materials* 26, no. 48 (2014): 8163–8168, <https://doi.org/10.1002/adma.201402847>.
5. H. Li, Y. Tan, P. Liu, et al., “Atomic-Sized Pores Enhanced Electrocatalysis of TaS₂ Nanosheets for Hydrogen Evolution,” *Advanced Materials* 28, no. 40 (2016): 8945–8949, <https://doi.org/10.1002/adma.201602502>.
6. Y. Feng, S. Gong, E. Du, et al., “3R TaS₂ Surpasses the Corresponding 1T and 2H Phases for the Hydrogen Evolution Reaction,” *Journal of Physical Chemistry C* 122, no. 4 (2018): 2382–2390, <https://doi.org/10.1021/acs.jpcc.7b10833>.
7. B. Chamlagain, Q. Cui, S. Paudel, M. M. C. Cheng, P. Y. Chen, and Z. Zhou, “Thermally Oxidized 2D TaS₂ as a High-κ Gate Dielectric for MoS₂ Field-Effect Transistors,” *2D Materials* 4, no. 3 (2017): 031002, <https://doi.org/10.1088/2053-1583/aa780e>.
8. X. Liu, J. Gu, K. Ding, et al., “Photoresponse of an Organic Semiconductor/Two-Dimensional Transition Metal Dichalcogenide Heterojunction,” *Nano Letters* 17, no. 5 (2017): 3176–3181, <https://doi.org/10.1021/acs.nanolett.7b00695>.
9. D. Stolovas, R. Popovitz-Biro, S. S. Sinha, et al., “Electrical Properties of LaS-TaS₂ Misfit Layered Compound Nanotubes,” *Israel Journal of Chemistry* 62, no. 3-4 (2022): e202100072, <https://doi.org/10.1002/ijch.202100072>.
10. C. Drivas, F. Iacovella, G. Deligeorgis, and S. Kennou, “Electronic Properties of the Poly(3-hexylthiophene)/MoS₂ Interfaces: The Influence of the Substrate,” *Applied Surface Science* 572 (2022): 151372, <https://doi.org/10.1016/j.apsusc.2021.151372>.
11. C. Drivas, S. Kennou, and G. Kyriakou, “Phthalocyanine Interfaces With MoS₂ (0001): The Effect of the Metal Centre on the Charge Transfer,” *Applied Surface Science* 682 (2025): 161672, <https://doi.org/10.1016/j.apsusc.2024.161672>.
12. S. Nagata, T. Aochi, T. Abe, et al., “Superconductivity in the Layered Compound 2H-TaS₂,” *Journal of Physics and Chemistry of Solids* 53, no. 10 (1992): 1259–1263, [https://doi.org/10.1016/0022-3697\(92\)90242-6](https://doi.org/10.1016/0022-3697(92)90242-6).
13. W. Shi, J. Ye, Y. Zhang, et al., “Superconductivity Series in Transition Metal Dichalcogenides by Ionic Gating,” *Scientific Reports* 5, no. 1 (2015): 12534, <https://doi.org/10.1038/srep12534>.
14. R. Niu, J. Li, W. Zhen, et al., “Enhanced Superconductivity and Critical Current Density due to the Interaction of InSe₂ Bonded Layer in (InSe₂)_{0.12}NbSe₂,” *Journal of the American Chemical Society* 146, no. 2 (2024): 1244–1249, <https://doi.org/10.1021/jacs.3c09756>.
15. A. D. Yoffe, “Electronic Properties of Some Chain and Layer Compounds,” *Chemical Society Reviews* 5 (1976): 51, <https://doi.org/10.1039/cs9760500051>.
16. H. P. Hughes and R. A. Pollak, “Charge Density Waves in Layered Metals Observed by X-Ray Photoemission,” *Philosophical Magazine* 34, no. 6 (1976): 1025–1046, <https://doi.org/10.1080/00318087608227726>.
17. J. M. Pereira, D. Tezze, B. Martín-García, et al., “Enhanced Superconductivity in 2H-TaS₂ Devices Through in Situ Molecular Intercalation,” *ACS Applied Materials & Interfaces* 16, no. 31 (2024): 41626–41632, <https://doi.org/10.1021/acsami.4c04997>.
18. J. Shi, X. Wang, S. Zhang, et al., “Two-Dimensional Metallic Tantalum Disulfide as a Hydrogen Evolution Catalyst,” *Nature*

- Communications* 8, no. 1 (2017): 958, <https://doi.org/10.1038/s41467-017-01089-z>.
19. S. Chiang, G. K. Wertheim, and F. J. DiSalvo, "Many-Electron Screening in Narrow-Band Metals; XPS in Layered Dichalcogenides," *Solid State Communications* 19, no. 1 (1976): 75–78, [https://doi.org/10.1016/0038-1098\(76\)91733-6](https://doi.org/10.1016/0038-1098(76)91733-6).
 20. D. J. Morgan, "XPS Insights: Asymmetric Peak Shapes in XPS," *Surface and Interface Analysis* 55, no. 8 (2023): 567–571, <https://doi.org/10.1002/sia.7215>.
 21. S. Hüfner and G. K. Wertheim, "Core-Line Asymmetries in the X-Ray-Photoemission Spectra of Metals," *Physical Review B* 11, no. 2 (1975): 678–683, <https://doi.org/10.1103/PhysRevB.11.678>.
 22. S. Hüfner, G. K. Wertheim, and J. H. Wernick, "XPS Core Line Asymmetries in Metals," *Solid State Communications* 17, no. 4 (1975): 417–422, [https://doi.org/10.1016/0038-1098\(75\)90468-8](https://doi.org/10.1016/0038-1098(75)90468-8).
 23. D. Ganta, S. Sinha, and R. T. Haasch, "2-D Material Molybdenum Disulfide Analyzed by XPS," *Surface Science Spectra* 21, no. 1 (2014): 19–27, <https://doi.org/10.1116/11.20140401>.
 24. C. Liu, C. Fu, L. Tang, et al., "Molecule-Based Vertical Transistor via Intermolecular Charge Transport Through π - π Stacking," *Nano Research* 17, no. 5 (2024): 4573–4581, <https://doi.org/10.1007/s12274-023-6252-3>.
 25. B. M. Kumar, C. Malavika, and E. S. Kannan, "Defect-Engineered Resistive Switching in van der Waal Metals," *IEEE Transactions on Electron Devices* 71, no. 11 (2024): 7144–7148, <https://doi.org/10.1109/TED.2024.3457730>.
 26. Y. Hao, H. Xu, Z. Lv, et al., "Lattice-Confined Localized Alloying of Bi_{0.67}Ta_{0.33} Anode Enabling Ultrafast and Stable Sodium Storage Up to 150 °C," *Chemical Engineering Journal* 496 (2024): 153876, <https://doi.org/10.1016/j.cej.2024.153876>.
 27. Y. Bao, J. Deng, K. Ma, R. Wang, J. Wu, and Y. Lu, "Thick-Film Printing of TaS₂ Soft Films on the Textured Surface to Enhance Wear Life," *Surface and Coating Technology* 476 (2024): 130231, <https://doi.org/10.1016/j.surfcoat.2023.130231>.
 28. Q. He, K. Si, Z. Xu, et al., "Direct synthesis of Controllable Ultrathin Heteroatoms-Intercalated 2D Layered Materials," *Nature Communications* 15, no. 1 (2024): 6320, <https://doi.org/10.1038/s41467-024-50694-2>.
 29. Z. Han, X. Han, S. Wu, et al., "Phase and Composition Engineering of Self-Intercalated 2D Metallic Tantalum Sulfide for Second-Harmonic Generation," *ACS Nano* 18, no. 8 (2024): 6256–6265, <https://doi.org/10.1021/acsnano.3c10383>.
 30. F. Deng, Z. Zhang, X. Xu, et al., "2D Tantalum Disulfide Reduction Strategy Customized Ta₂O₅/rGO Heterointerface Aerogel Toward Boosting Electromagnetic Wave Absorption and Flame Retardancy," *Small* 4 (2024): 2311818, <https://doi.org/10.1002/sml.202311818>.
 31. M. A. Baker, R. Gilmore, C. Lenardi, and W. Gissler, "XPS Investigation of Preferential Sputtering of S From MoS₂ and Determination of MoS_x Stoichiometry From Mo and S Peak Positions," *Applied Surface Science* 150, no. 1 (1999): 255–262, [https://doi.org/10.1016/S0169-4332\(99\)00253-6](https://doi.org/10.1016/S0169-4332(99)00253-6).
 32. M. J. Acres, H. Hussain, M. S. Walczak, et al., "Core Level Photoemission Line Shape Selection: Atomic Adsorbates on Iron," *Surface and Interface Analysis* 52, no. 8 (2020): 507–512, <https://doi.org/10.1002/sia.6770>.
 33. W. M. Skinner, H. W. Nesbitt, and A. R. Pratt, "XPS Identification of Bulk Hole Defects and Itinerant Fe 3d Electrons in Natural Troilite (FeS)," *Geochimica et Cosmochimica Acta* 68, no. 10 (2004): 2259–2263, <https://doi.org/10.1016/j.gca.2003.11.026>.
 34. X. Crispin, S. Marciniak, W. Osikowicz, et al., "Conductivity, Morphology, Interfacial Chemistry, and Stability of Poly(3,4-ethylene dioxythiophene)-Poly(styrene sulfonate): A Photoelectron Spectroscopy Study," *Journal of Polymer Science Part B: Polymer Physics* 41, no. 21 (2003): 2561–2583, <https://doi.org/10.1002/polb.10659>.
 35. J. C. Dupin, D. Gonbeau, I. Martin-Litas, P. Vinatier, and A. Levasseur, "Amorphous Oxysulfide Thin Films MOySz (M=W, Mo, Ti) XPS Characterization: Structural and Electronic Peculiarities," *Applied Surface Science* 173, no. 1-2 (2001): 140–150, [https://doi.org/10.1016/S0169-4332\(00\)00893-X](https://doi.org/10.1016/S0169-4332(00)00893-X).
 36. L. Sygellou, "An In-Situ Photoelectron Spectroscopy Study of the Thermal Processing of Ammonium Tetrathiomolybdate, (NH₄)₂MoS₄, Precursor," *Applied Surface Science* 476 (2019): 1079–1085, <https://doi.org/10.1016/j.apsusc.2019.01.193>.
 37. L. Sygellou, "Study of the Thermal Decomposition of Ammonium Tetrathiomolybdate, (NH₄)₂MoS₄, in H₂ and H₂O Media by Quasi In-Situ Photoelectron Spectroscopy (XPS/UPS)," *Applied Surface Science* 682 (2025): 161644, <https://doi.org/10.1016/j.apsusc.2024.161644>.
 38. R. S. C. Smart, W. M. Skinner, and A. R. Gerson, "XPS of Sulfide Mineral Surfaces: Metal-Deficient, Polysulfides, Defects and Elemental Sulphur," *Surface and Interface Analysis* 28, no. 1 (1999): 101–105, [https://doi.org/10.1002/\(SICI\)1096-9918\(199908\)28:1<101::AID-SIA627>3.0.CO;2-O](https://doi.org/10.1002/(SICI)1096-9918(199908)28:1<101::AID-SIA627>3.0.CO;2-O).
 39. A. R. Pratt, I. J. Muir, and H. W. Nesbitt, "X-ray Photoelectron and Auger Electron Spectroscopic Studies of Pyrrhotite and Mechanism of Air Oxidation," *Geochimica et Cosmochimica Acta* 58, no. 2 (1994): 827–841, [https://doi.org/10.1016/0016-7037\(94\)90508-8](https://doi.org/10.1016/0016-7037(94)90508-8).
 40. C. Palacio and J. M. Martínez-Duart, "EELS and Low-Energy Electron Emission of Clean and Oxygen-Exposed Tantalum," *Surface and Interface Analysis* 15, no. 11 (1990): 675–680, <https://doi.org/10.1002/sia.740151107>.
 41. M. A. Isaacs, P. R. Davies, A. Graf, D. J. Morgan, and R. Palgrave, "XPS Insight Note: Coster-Kronig Broadening," *Surface and Interface Analysis* 57, no. 7 (2025): 548–554, <https://doi.org/10.1002/sia.7410>.
 42. J. A. Bearden and A. F. Burr, "Reevaluation of X-Ray Atomic Energy Levels," *Reviews of Modern Physics* 39, no. 1 (1967): 125–142, <https://doi.org/10.1103/RevModPhys.39.125>.
 43. P. Buabthong, N. Becerra Stasiewicz, S. Mitrovic, and N. S. Lewis, "Vanadium, Niobium and Tantalum by XPS," *Surface Science Spectra* 24, no. 2 (2017): 024001, <https://doi.org/10.1116/1.4998018>.
 44. A. H. Reshak, "Full-Potential Calculations of the Electronic and Optical Properties of 1T and 2H Phases of TaS₂ Intercalated With Lithium," *Physica B: Condensed Matter* 373, no. 1 (2006): 1–7, <https://doi.org/10.1016/j.physb.2005.10.103>.
 45. M. C. Biesinger, B. P. Payne, A. P. Grosvenor, L. W. M. Lau, A. R. Gerson, and R. S. C. Smart, "Resolving Surface Chemical States in XPS Analysis of First Row Transition Metals, Oxides and Hydroxides: Cr, Mn, Fe, Co and Ni," *Applied Surface Science* 257, no. 7 (2011): 2717–2730, <https://doi.org/10.1016/j.apsusc.2010.10.051>.
 46. C. D. Wagner, L. E. Davis, M. V. Zeller, J. A. Taylor, R. H. Raymond, and L. H. Gale, "Empirical Atomic Sensitivity Factors for Quantitative Analysis by Electron Spectroscopy for Chemical Analysis," *Surface and Interface Analysis* 3, no. 5 (1981): 211–225, <https://doi.org/10.1002/sia.740030506>.
 47. C. D. Wagner, "Sensitivity Factors for XPS Analysis of Surface Atoms," *Journal of Electron Spectroscopy and Related Phenomena* 32, no. 2 (1983): 99–102, [https://doi.org/10.1016/0368-2048\(83\)85087-7](https://doi.org/10.1016/0368-2048(83)85087-7).